IOP Conference Series: Materials Science and Engineering

Aberration effects in quick X-Ray reflectivity of curved samples

Aberration effects in quick X-Ray reflectivity of curved samples

Krassimir Stoev[1], Kenji Sakurai * [2]

[1] AECL – Chalk River Laboratories, Chalk River, Ontario K0J 1J0, Canada

[2] National Institute for Materials Science, 1-2-1 Sengen, Tsukuba, Ibaraki, Japan

*Corresponding author: sakurai@yuhgiri.nims.go.jp

Abstract. Quick x-ray reflectivity (QXRR) is a new surface examination technique for studying fast processes at the surface and interface of the materials on a nano-scale. The currently available models for classical scanning-type x-ray reflectivity cannot be applied directly to the QXRR simulations. The present article proposes and discusses models for simulation of QXRR measurements of curved samples, which are applicable for analysis of liquid materials.

1. Introduction

X-ray reflectivity is a non-destructive testing technique used to investigate the structure of surfaces, thin films (including multilayers), or buried interfaces (depth profiling), and for studying the processes occurring at surfaces and interfaces such as adsorption, adhesion and interdiffusion. Classical x-ray reflectivity is a relatively slow technique, with a typical time for one scan on the order of hours. Recently, a new experimental setup for quick x-ray reflectivity (QXRR) was proposed [1-3] based on Naudon's method [4-9]. This new technique appears promising, because it will permit the study of fast processes at the surface and interfaces of materials on a nano-scale. The new setup for quick x-ray reflectometry will allow measurements to be done within seconds, thus permitting studies of the time evolution of chemical, thermal, and mechanical changes at the surface and interface of different materials.

Current models for interpretation of x-ray reflectivity data are derived for the classical x-ray reflectivity setup, where both the incident and the detected beams are restricted by slits. These models are not directly applicable to quick x-ray reflectivity simulations, because they do not account for the contribution of diffuse scattering, nor for the extended source size and for the curvature of the sample. Quick x-ray reflectivity utilizes an extended x-ray source, and the measurement setup does not include a detector slit, so both specular reflectivity and diffuse scattering associated with different points of the source can reach the detector. A model accounting for the contribution of diffuse scattering to the measured data for quick x-ray reflectivity was presented in [10]. In this work, we extend the normalization model for flat samples presented in [6], and propose models for evaluation of the contribution of the sample curvature to measured signal for QXRR.

2. Description of experimental setup for quick x-ray reflectivity

A schematic of the setup for quick x-ray reflectivity of flat samples is presented in Figure 1. In contrast to classical x-ray reflectivity techniques, the QXRR experimental setup utilises an extended linear monochromatic source (on the order of 10 mm in height, which supplies a beam with incident angles in the range 0 to 40 mrad on the sample). The source is assumed to be homogeneous and isotropic. The beam is restricted with a slit-knife, and the reflected divergent beam is detected by a position-sensitive detector like a linear pixel array or an imaging plate. For simplicity, we will consider only linear pixel detectors in our model.

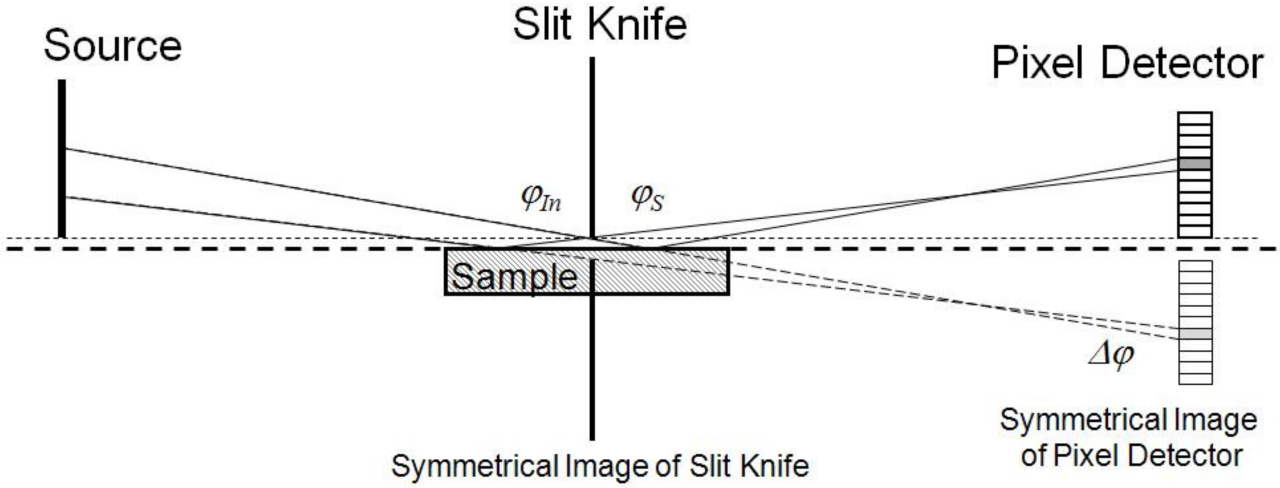

Figure 1. Schematic representation of quick x-ray reflectivity setup (φ_{In} and φ_S are the incident and scattering angles, and $\Delta\varphi$ is the acceptance angle for the detector pixel).

3. Modeling of quick x-ray reflectivity of curved samples

The QXRR schematic used for modeling curved samples is shown in Figure 2. For simplicity, it was assumed that the slit-knife is centered above the top point of the samples, but that the sample can have different lengths to the left and to the right of the slit-knife, e.g., we did not consider cases when the slit-knife is offset in respect to the top position of the curved sample.

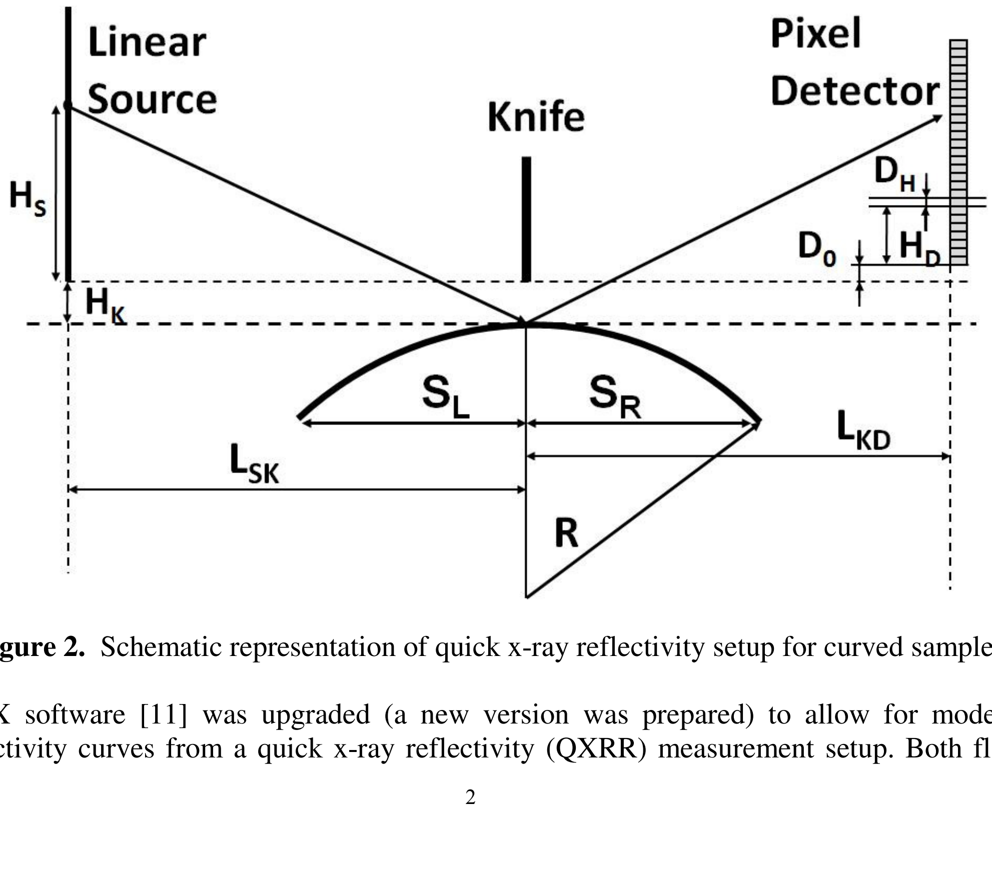

Figure 2. Schematic representation of quick x-ray reflectivity setup for curved samples.

The RefleX software [11] was upgraded (a new version was prepared) to allow for modeling of x-ray specular reflectivity curves from a quick x-ray reflectivity (QXRR) measurement setup. Both flat and curved (convex) sample shapes were included. The software allows for modeling of single interfaces or multi-layered structures. The x-ray reflectivity calculation model was validated against other software packages [12-14] using several sample models.

The following parameters were used during the modeling presented in this paper: the source had height of 10 mm and width of 0.05 mm, and the source energy was 8.04 keV (Cu-Kα); the detector was assumed to be 1024 pixels photodiode array, each pixel has a height of D_H = 0.05 mm and width of 2.5 mm; the distance source-to-knife was assumed to be L_{SK} = 270 mm, and the distance from the knife to the detector was assumed to be L_{DK} = 1812 mm; the clearance between the knife edge and the sample surface was assumed to be H_K = 0.03 mm for most of the calculations. The other parameters, e.g., sample length to the left and right of the slit-knife and radius of sample curvature (S_L, S_R, R), and in some cases H_K, were varied during the calculations. In the presented models, an ideal detector was considered, e.g., the spatial resolution of the detector was not considered.

A simplified model for correcting the x-ray reflectivity from flat samples in the case of QXRR was presented in [6]. Several publications have previously presented models for calculating x-ray reflectivity from curved samples for the case of classical x-ray reflectivity [15-17]. Unfortunately, the above-mentioned models cannot be applied directly to the case of quick x-ray reflectivity of curved samples, because they do not account for the sample curvature [6] or for the extended source used in QXRR [15-17]. In order to overcome these deficiencies, four different calculation models were proposed and implemented in the RefleX software:

- Model #1: Flat sample with inherent divergence included (to account for the extended source), and with added external divergence to account for the sample curvature;
- Model #2: 2D model for a cylindrical convex sample (axis of the cylinder is perpendicular to the incidence plane), without accounting for the aberrations and distortions of the source image;
- Model #3: Numerical integration of a 2D cylindrical convex sample, with calculations carried out simultaneously for flat and curved samples;
- Model #4: 3D model for a spherical convex sample, accounting for the astigmatism/aberrations and distortions of the source image.

The models were introduced in order of increasing the precision of describing the process of propagation of x-rays trough the system. Models #1 and #2 are very simple and allow for very fast calculations, which is important when these models are used for fitting of experimental data (the fitting algorithms usually require many calculations of the reflectivity curve in order to determine the optimal structural parameters of the sample). Models #3 and #4 are based on numerical integration, so they are considerably slower than Models #1 and #2, and are less suitable for application if fitting algorithms. Model #4 should be considered the most-precise model (and correspondingly the slowest model), which best describes the effects of the sample curvature on the reflectivity scans. Model #4 should be used for evaluating the validity of the other models.

The proposed models were used for calculating x-ray reflectivity of convex samples and parametric studies of the influence of the different sample parameters on the x-ray reflectivity curves. Three types of curved samples were considered: liquid Ga (gallium) sample; single Au (gold) layer (15 nm) on a Si (silicon) substrate; and multilayer sample (30 bi-layers of Ni(nickel, 3 nm)/C(carbon, 3 nm) on a Si substrate). Most of the comparisons in this paper are based on the liquid Ga sample, which is the simplest sample, and for which there are no fringes in the reflectivity scan, and only the region around the critical angle of reflection is of importance.

3.1. Model #1: Flat sample with external divergence

For each detector pixel, a single source point was calculated corresponding to reflection from the sample point directly under the slit-knife, and the reflectivity was calculated for this source point. After that, the flat-sample model applied the following corrections to the theoretical reflectivity curve:

- A correction for the acceptance angle of the detector. If the projection of the sample onto the detector plane (as seen from the source point), is smaller than the size of the detector pixel, the acceptance angle is effectively reduced. This projection will also be corrected for the fact that the beam is at an angle (i.e., not strictly perpendicular) to the projection, and that the slit-knife can effectively lead to a reduction of the usable sample length.

- A correction for the fact that there is more than one source point contributing to each detector pixel, i.e., correction for the source length visible from each detector pixel, which also can be represented as the ration between the detector pixel acceptance angle for flat and curved samples.
- A correction for the inherent source divergence. We can determine the total number of detector pixels visible from a source point, and use this to calculate the convolution of the reflectivity curve (i.e., this is essentially loss of angular resolution due to the fact that the projection of the slit-knife or sample length could be bigger than the detector pixel size; in other words, the reflection from one "source pixel" spreads over several detector pixels).
- If selected, an additional correction in which convolution of the reflectivity curve is performed based on the specified external divergence, as a simplified approximation of the sample curvature.

This model is a generalization of Naudon's model [6], which only corrected for the extended source length contribution to each detector point, and did not consider the size of the detector pixel (i.e., the Naudon model [6] used only the second of the above-listed corrections). Model #1 is used for normalization of the results from the other models. An example of the dependence of the shape of the reflectivity curve on the sample size for a flat Ga sample is shown in Figure 3. The same results were obtained by using Model #3 and Model #4 (numerical integration over the sample length), which confirms the validity of both models. As can be seen, the reduction in sample length leads to suppression of the x-ray reflectivity intensity, especially in the low-angle region. The direct radiation which can hit the detector at very low incident angles and which can be used for sample adjustment and determination of the zero-angle position (as per [4]), was not considered in any of the models.

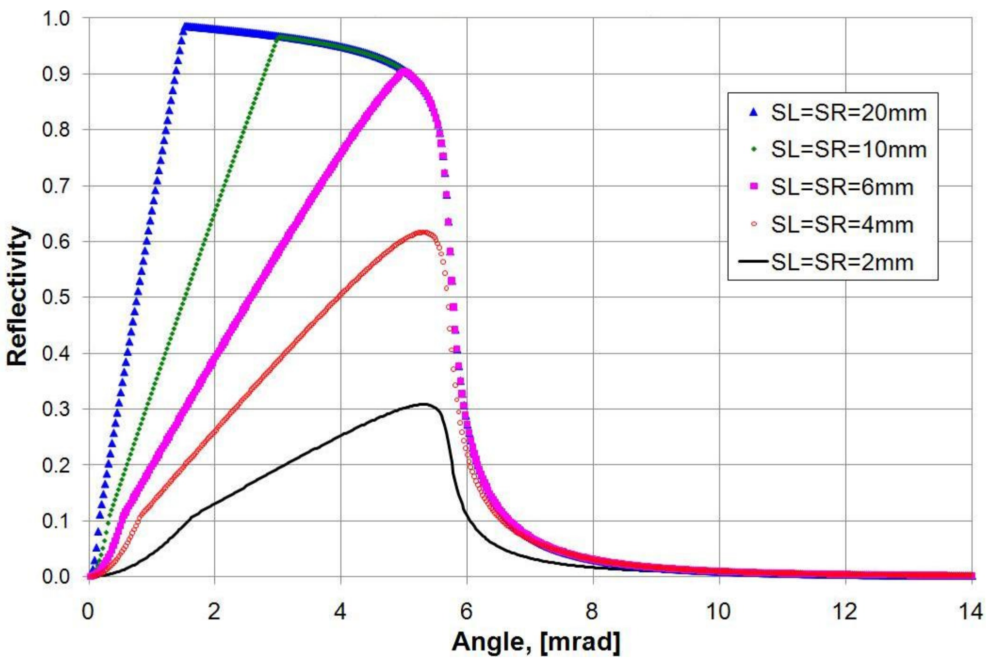

Figure 3. Effect of the sample size on x-ray reflectivity for flat Ga sample ($\boldsymbol{E}$ = 8.04 keV, $\boldsymbol{H_K}$ = 0.03 mm, no roughness).

The simplest way to model sample curvature is to add divergence to the reflected beam, thus simulating a convex sample. For the specific geometry which was modeled, the effect of inherent angular divergence (e.g., the fact that one source point can contribute to several detector pixels) was very small, and not visible if plotted on a linear scale. The effect of external divergence on the shape of the reflectivity curve is shown in Figure 4. As can be seen, external divergence leads to broadening of the sharp transition region in the reflectivity curve around the critical angle, and could lead to misinterpretation of the position of the critical angle for the selected material. The overall conclusion is that this model is too simplistic (when compared to the results from Model #4, this model cannot correctly predict the shape of the reflectivity curve) and cannot be used for fitting experimental data and extracting sample parameters. This is mainly due to the fact that Model #1 uses one and the same external divergence for all source points, which is not a realistic representation of the effect of the sample curvature on the reflectivity curve.

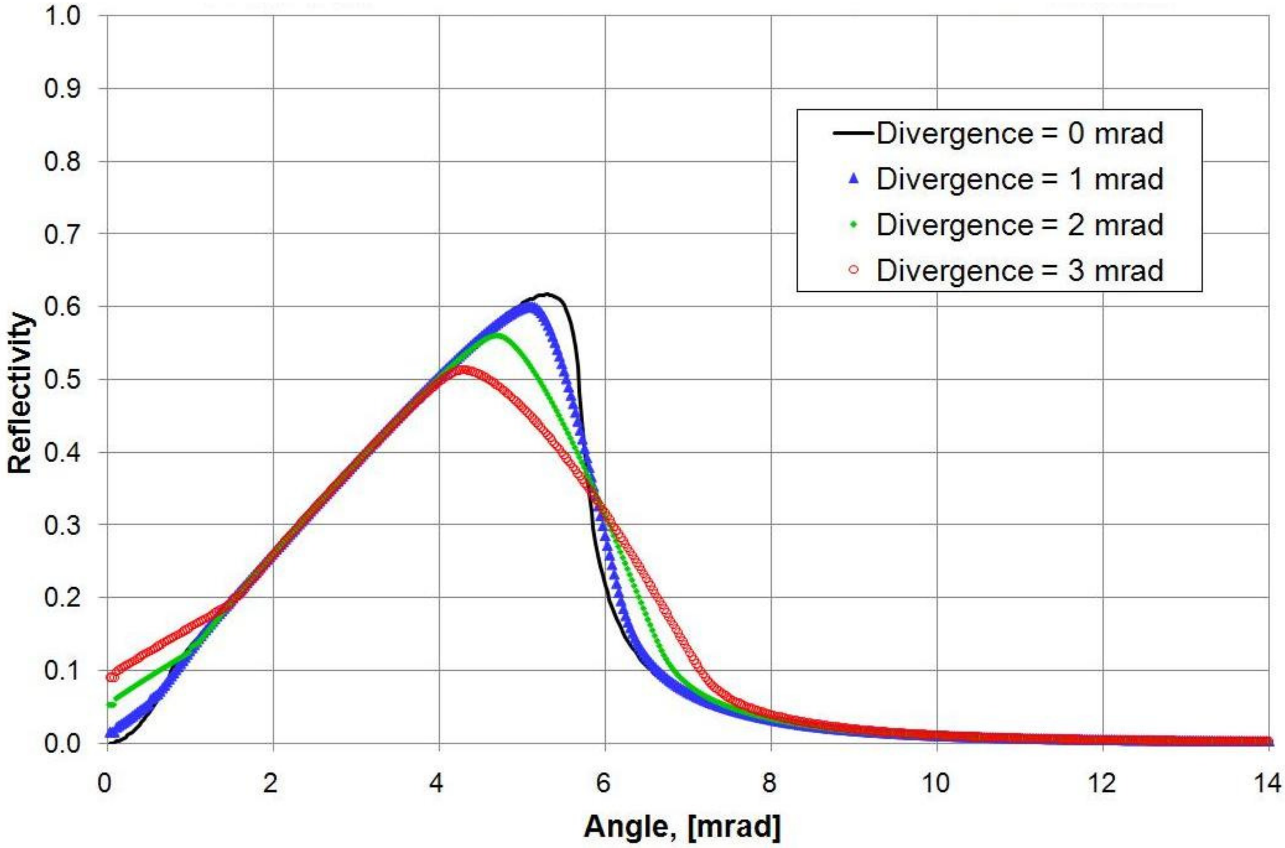

Figure 4. Effect of the external divergence on the x-ray reflectivity curve for flat Ga sample ($\boldsymbol{E}$ = 8.04 keV, $\boldsymbol{S_L} = \boldsymbol{S_R}$ = 4 mm, $\boldsymbol{H_K}$ = 0.03 mm, no roughness).

3.2. Model #2: Simplified 2D model for cylindrical convex sample

For the 2D cylindrical convex sample, we can follow the same procedure as for the flat sample. Again, for each detector pixel, a single source point was calculated corresponding to reflection from the sample point directly under the slit-knife, and the reflectivity was calculated for this source point. After that the following corrections were applied to the calculated reflectivity:

- A correction for the size of the source, i.e., height of the source region, which contributes to the specular reflection for the corresponding detector pixel.
- A correction to the acceptance angle of the detector. If the projection of the sample/slit onto the detector plane (as seen from the source pint) is smaller than the size of the detector pixel, the acceptance angle is effectively reduced.
- A correction for the inherent angular divergence for each source point (i.e., the total number of detector pixels visible from a source point). This is used for applying convolution to the final results for the reflectivity curve.

The effect of sample radius on the shape of the reflectivity curve, as calculated by using Model #2, is shown in Figure 5. When compared to the results from the more-precise models (Models #3 and #4), this model cannot describe correctly the changes in the reflectivity curve due to sample curvature. Again, this model, although very convenient, over-simplifies the propagation of x-rays through the experimental setup, and cannot be used for fitting experimental data (i.e., when the results from Model #2 are compared to the results from Model #4, Model #2 cannot correctly predict the shape of the reflectivity curve).

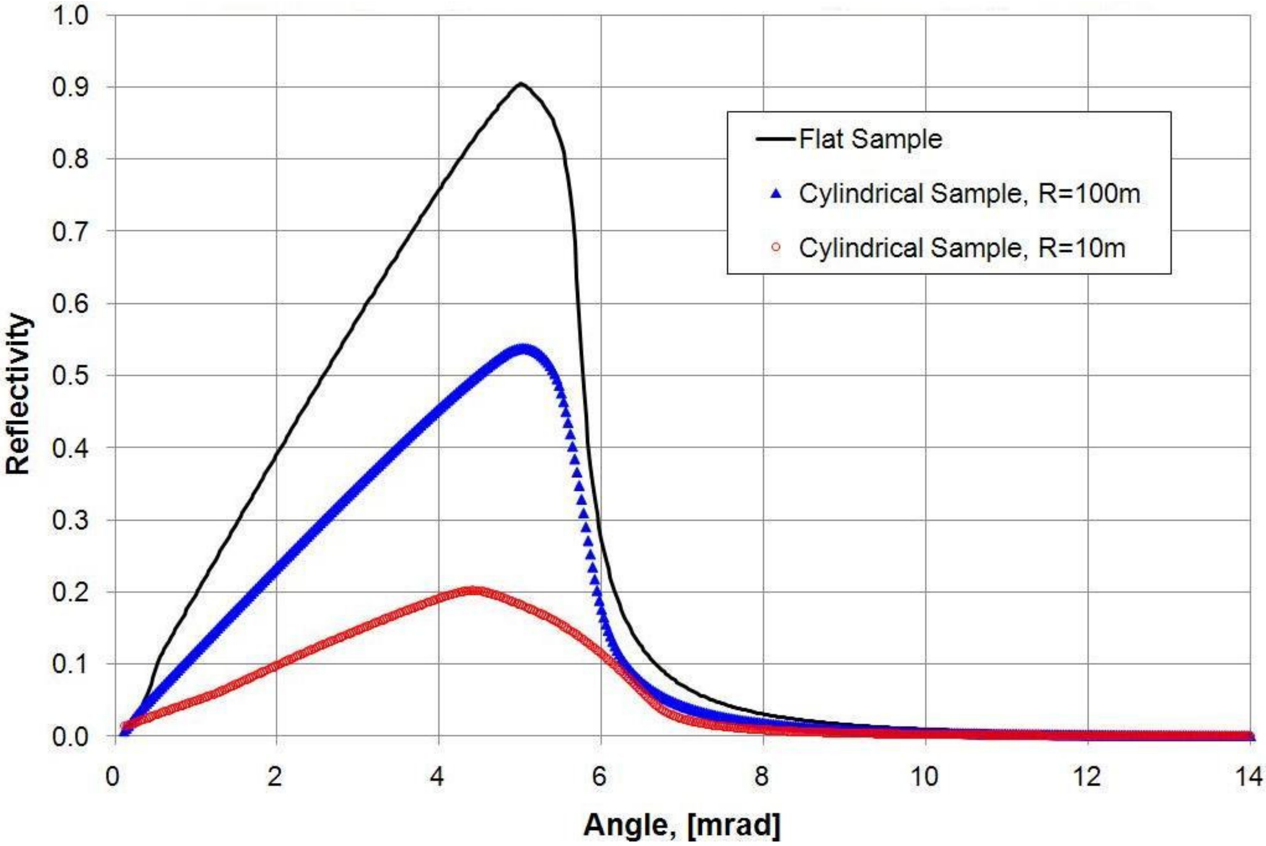

Figure 5. Effect of changing the sample radius on the x-ray reflectivity curve for Ga sample for Model #2 ($\boldsymbol{E}$ = 8.04 keV, $\boldsymbol{S_L} = \boldsymbol{S_R}$ = 6 mm, $\boldsymbol{H_K}$ = 0.03 mm, no roughness).

3.3. Model #3: Numerical integration of 2D cylindrical convex sample

This model uses numerical integration over the whole sample for each detector point. The sample is assumed to be a cylindrical mirror and is divided in $\boldsymbol{N_S}$ sub-intervals (usually between 100 and 400), and for each detector pixel and each sample sub-interval, the corresponding source point and reflection angle is calculated, including corrections for the slit height and finite sample size (i.e., visibility corrections). For the difference from Model #2, this model uses the correct reflectivity and detector acceptance angle for each sub-interval, while Model #2 can be viewed as integration with $\boldsymbol{N_S}$ = 1, or one can think of it as if it uses on and the same reflectivity and detector acceptance angle for all sub-regions. Other way to compare Models #2 and #3 is to think of Model #2 as the results of applying a moving average over many points to the results from Model #3.

The calculations for Model #3 are done for both flat and curved samples. The results for the flat sample are normalized in such a way as to have the maximum in the reflection curve equal to the maximum in the reflection curve for Model #1. The results for the curved sample are normalized with the same normalization factor as the results for the flat sample. This method of normalization ensures that the limit conditions are satisfied (i.e., when the radius increases to infinity, the reflectivity of the curved sample becomes the same as the reflectivity of the flat sample). The effect of sample radius on the shape of the reflectivity curve is shown in Figure 6. As can be seen, the results from this model are significantly different than the results from Model #2. This difference is due to the fact that Model #2 does not account for different angular divergence for the different points of the source, i.e., Model #2 calculates a source range contributing to each detector pixel, but treats this as a single source point, which does not lead to a good approximation at glancing incidence angles (although similar approximations are used in the standard optics at normal incidence).

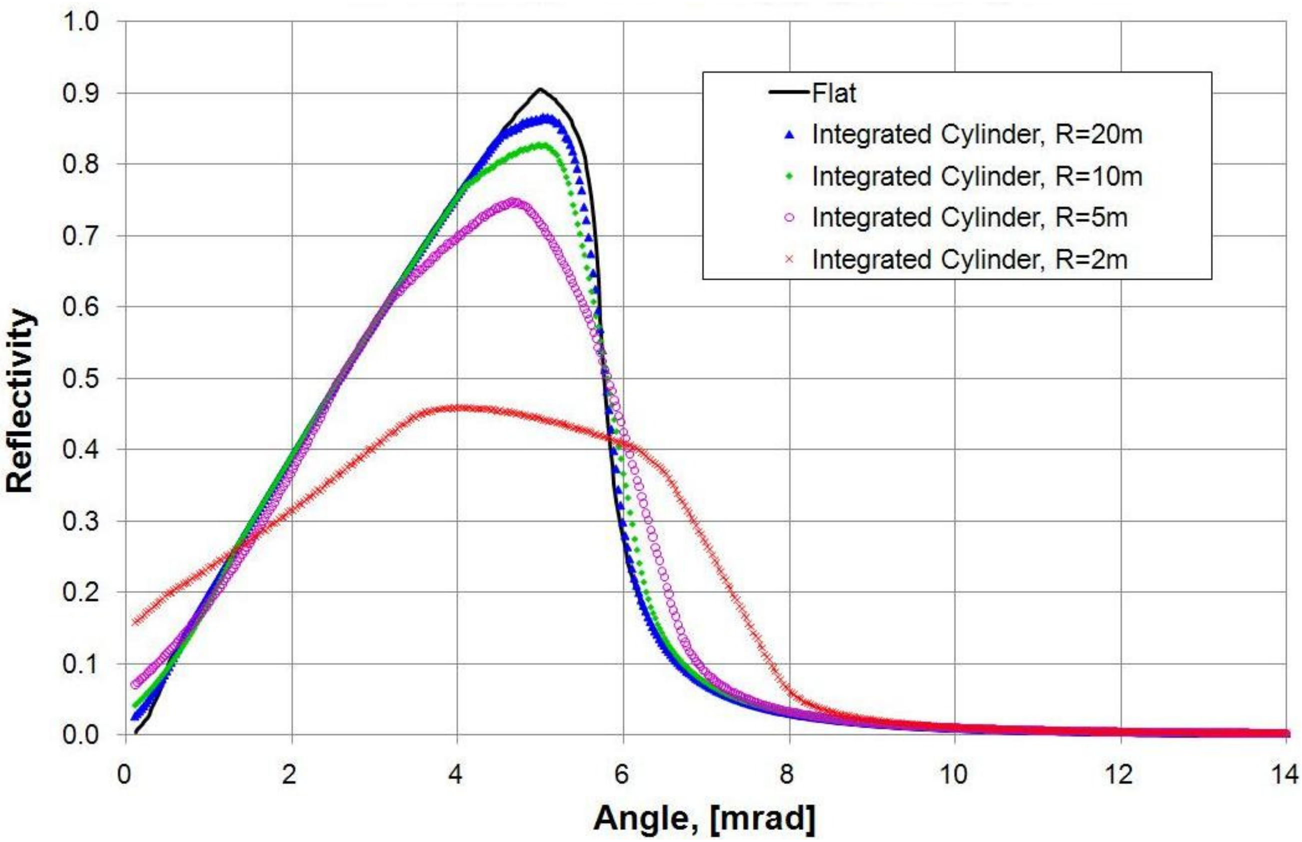

Figure 6. Effect of changing the sample radius on the x-ray reflectivity curve for Ga sample for Model #3 ($\boldsymbol{E}$ = 8.04 keV, $\boldsymbol{S_L} = \boldsymbol{S_R}$ = 6 mm, $\boldsymbol{H_K}$ = 0.03 mm, no roughness).

3.4. Model #4: 3D model for spherical convex sample

While Models #1 and #2 are very similar in the sense that they use a single sample point for each detector pixel and an average value over a range of source points, Model #3 uses different sub-sections of the sample with the corresponding source points, but does not consider the angular divergence of the beam within the sub-sections of the sample. In order to account for this difference, and also to account for the spherical shape of the sample, one needs a 3D model. For spherical samples at glancing incidence, because the source is very close to the sample, one has to consider the very strong aberrations in forming the source image. Discussion on this subject can be found in [15-17]. In this case, we can consider the sample as a convex mirror, which forms an image of the source. Due to the strong aberration effects, the image of the line source will not be a line, but will have a complex 3D shape, i.e., it will be blurred. Generally speaking, there will be two images formed (see Figure 7): one by the rays parallel to the incidence plane (tangential image); and one by the rays perpendicular to the incidence plane (sagittal image). The standard formulas [15-17] for the sagittal and tangential images are ($\boldsymbol{d_0}$, $\boldsymbol{d_S}$, $\boldsymbol{d_T}$, $\boldsymbol{\theta}$, and $\boldsymbol{R}$ are all positive, and are defined in Figure 7):

$$\frac{1}{d_0}-\frac{1}{d_S}=-\frac{2\cdot\sin(\theta)}{R}; \quad d_S=d_0\cdot\frac{1}{1+\dfrac{2\cdot d_0\cdot\sin(\theta)}{R}} \tag{1}$$

$$\frac{1}{d_0}-\frac{1}{d_T}=-\frac{2}{R\cdot\sin(\theta)}; \quad d_T=d_0\cdot\frac{1}{1+\dfrac{2\cdot d_0}{R\cdot\sin(\theta)}} \tag{2}$$

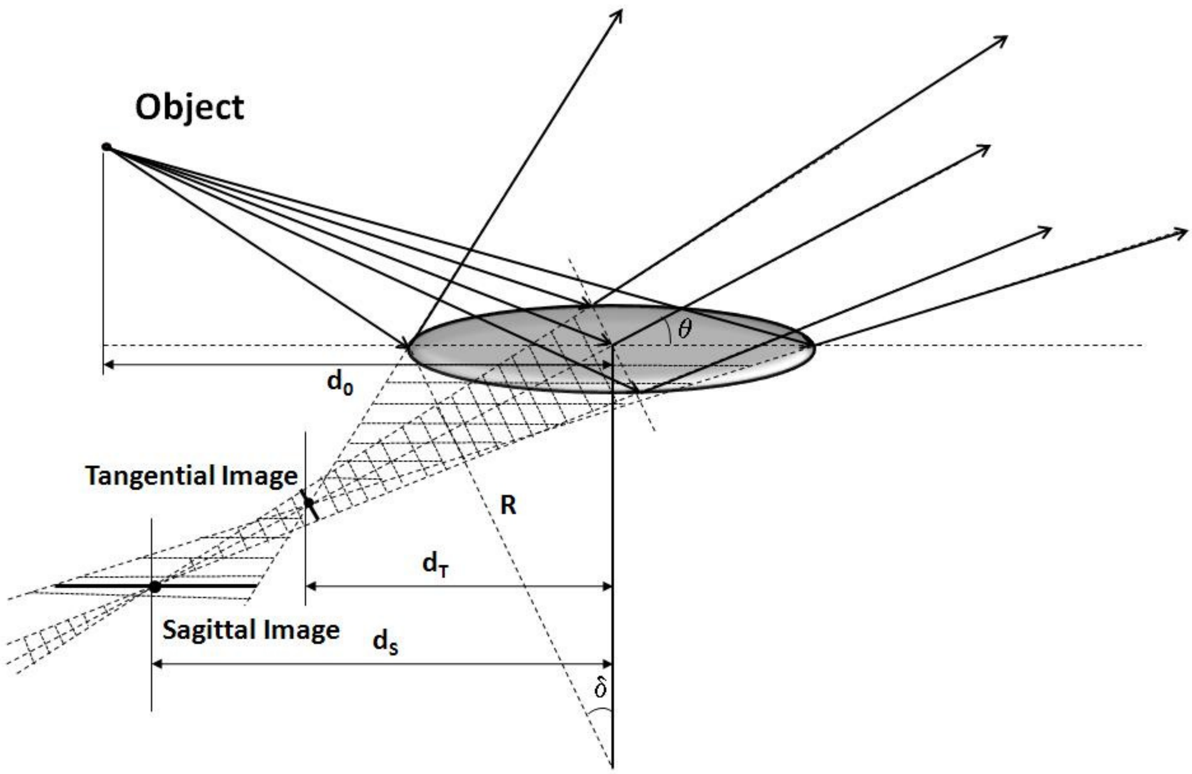

Figure 7. Formation of tangential and sagittal images at glancing incidence.

At glancing incidence, the sagittal image position does not change significantly with incident angle, i.e., there are no strong aberration effects in formation of the sagittal image. On the other hand, the position of the tangential image depends very strongly on the incident angle. The tangential image is the one that is of importance in QXRR simulations, because the sagittal rays practically do not contribute to the measured intensity due to the very long optical path employed in the measurement geometry and the limited width of the detector pixels. One has also to consider the fact that even the above formulas are approximations to the position of the images, and were developed for use in standard optics, which usually does not consider glancing incidence. For example, there are four tangential images of a line source presented in Figure 8: the first three are formed by the intersection points found by tracing three rays for three sample points (through the left, middle and right points of the mirror), while the fourth is the image position calculated using Equation 2. The center of the coordinate system was set at the center of the sample curvature. As can be seen, Equation 2 cannot predict the correct position of the tangential image at glancing incidence, and should not be used for modeling the sample curvature at glancing angles. Also, even ray-tracing produces multiple images depending on which part of the mirror is used. This result suggests that the mirror (sample) should be divided into small sub-sections, and the left and right ends of each sub-section should be used for calculation of the position of the tangential image. The calculated tangential images for different sample radii are shown in Figure 9. The center of the coordinate system was set at the center of the sample. As can be seen, the position of the tangential image depends very strongly on the radius of the sample. The smaller the sample radius, the closer is the image to the slit-knife, and the bigger is the acceptance angle for the slit-knife opening as visible from the source image (in comparison to the source image for a flat sample). This explains the stronger distortion of the reflectivity curve for small sample radius.

This model again uses numerical integration, i.e., the source is divided in small sub-sections (usually 1024, with each source sub-section replaced with a source point positioned in the middle of the sub-section). The sample is also divided in N_S sub-intervals (usually between 100 and 400), and for each source point and sample sub-section, the reflection angle, the tangential image, and the corresponding detector pixel are determined, and the calculated intensity is added to the total intensity for the corresponding detector pixel. The same calculations are carried out for a flat sample, for normalization purposes.

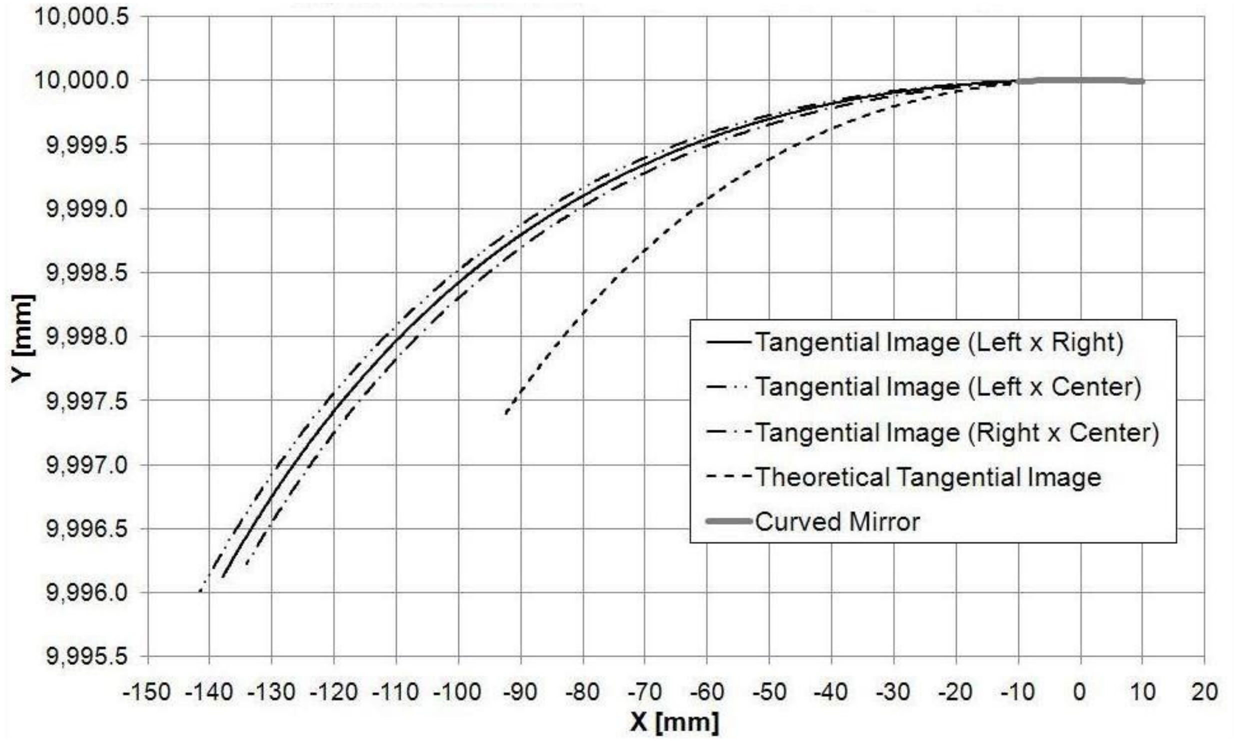

Figure 8. Tangential image formation for convex sample with radius $\boldsymbol{R}$ = 10 m.
(Left x Right) means that the image point is the intersection of rays from the left and right end of the mirror.
$\boldsymbol{S_L} = \boldsymbol{S_R}$ = 10 mm, sample center is at (0, 10000), source has coordinates (-270, 10000) – (-270, 10007.6).

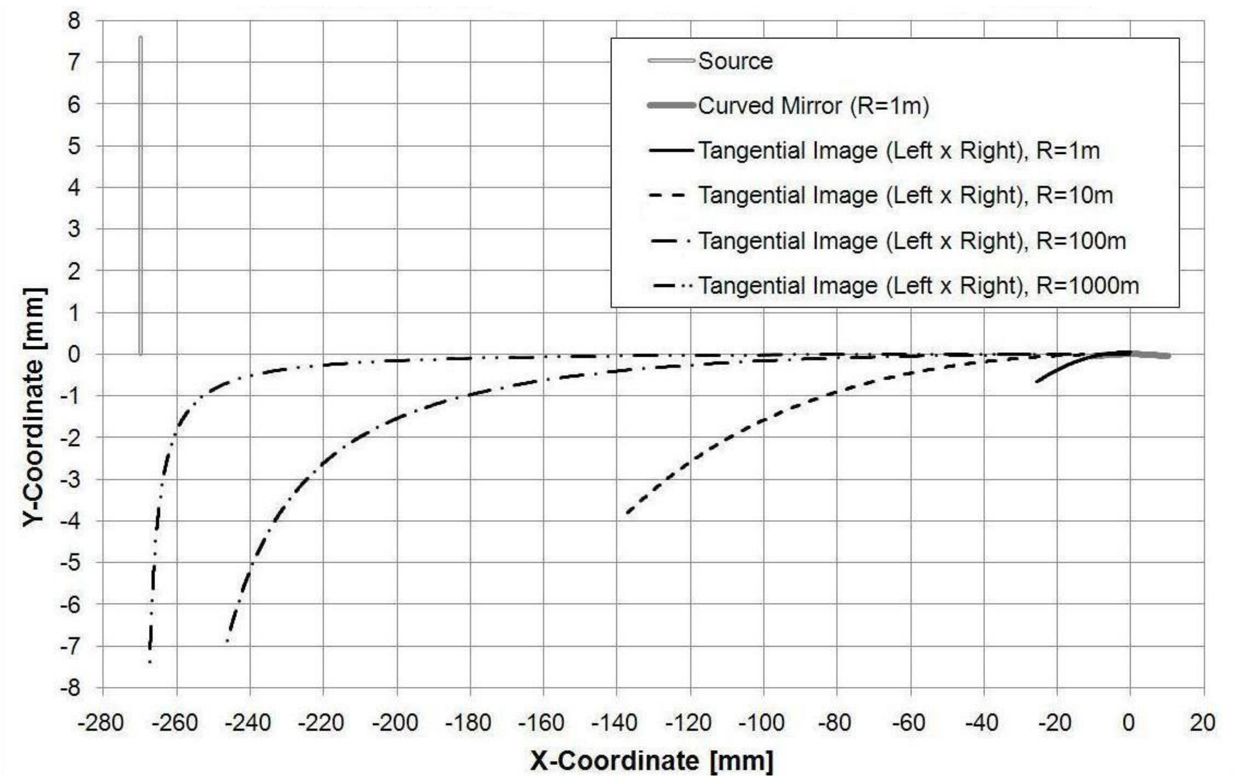

Figure 9. Tangential image formation for convex samples with different $\boldsymbol{R}$.
$\boldsymbol{S_L} = \boldsymbol{S_R}$ = 10 mm, sample center is at (0, 0), source has coordinates (-270, 0) – (-270, 7.6).

The sample sub-region acceptance angle from the source point, and the detector pixel acceptance angle from the tangential image point are calculated and used to normalize the detected energy in a manner similar to the one proposed in [17]. The final normalization was done in a manner similar to that used in Model #3 (i.e., the results for the flat sample are normalized in such a way as to have the same maximum in the reflection curve as the results for Model #1). The results for the curved sample are normalized with the same normalization factor as the results for the flat sample. The dependence of the reflectivity curve on the radius of sample curvature is shown in Figure 10. The results are very similar to those obtained with Model #3 and presented in Figure 6.

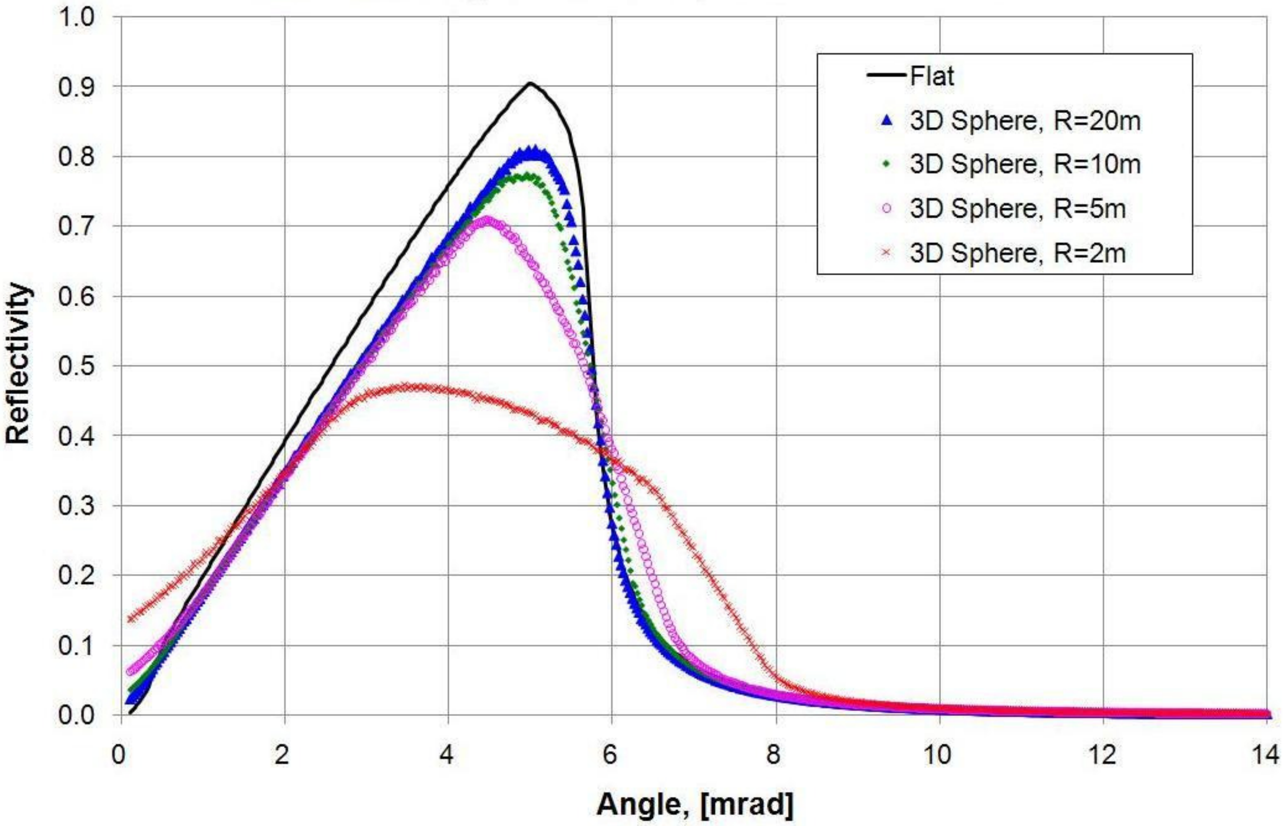

Figure 10. Effect of changing the sample radius on the x-ray reflectivity curve for Ga sample for Model #4 ($\boldsymbol{E}$ = 8.04 keV, $\boldsymbol{S_L} = \boldsymbol{S_R}$ = 6 mm, $\boldsymbol{H_K}$ = 0.03 mm, no roughness).

4. Discussion

As one can see, there are significant differences in the shape of the reflectivity curves produced by the different models. Model #3 (Integrated 2D Cylindrical) and Model #4 (3D Spherical) give somewhat similar results, and they can be considered the best models for description of the data. Model #4 was used further for simulation of other samples and should be used for fitting experimental results. Although this model is the slowest from calculation point of view, the differences in the shape of the reflectivity curves in comparison to the other models are big enough to justify the use of the slowest model.

The second sample modeled was a single 15 nm Au (gold) layer on a Si (silicon) substrate. The calculated reflectivity curves for samples with different radii are shown in Figure 11, in both linear and logarithmic scales. There are three effects that can be observed with the increase in curvature of the sample (i.e., with reduction of the sample radius):

- There is change in the region around the critical angle, which could be misinterpreted as change in the critical angle (e.g., sample density or roughness change);
- The intensity oscillations above the critical angle (e.g., Kiessig fringes, or thickness fringes) are blurred, i.e., the peak-to-valley amplitude of the oscillations is reduced;

- The maxima and the minima of the fringes are shifted toward higher angles, especially for the fringes immediately after the critical angle, which could lead to misinterpretation of the layer thickness or density.

Thus, sample curvature can significantly influence the interpretation of the results from QXRR, and that modeling to show the effect of curvature of the analysed sample is beneficial to the interpretation of experimental results. The best approach is to include the correction for the sample curvature (e.g., Model #3 or Model #4) in the fitting software, and to fit the sample curvature together with the other sample parameters when processing reflectivity curves from QXRR experiments.

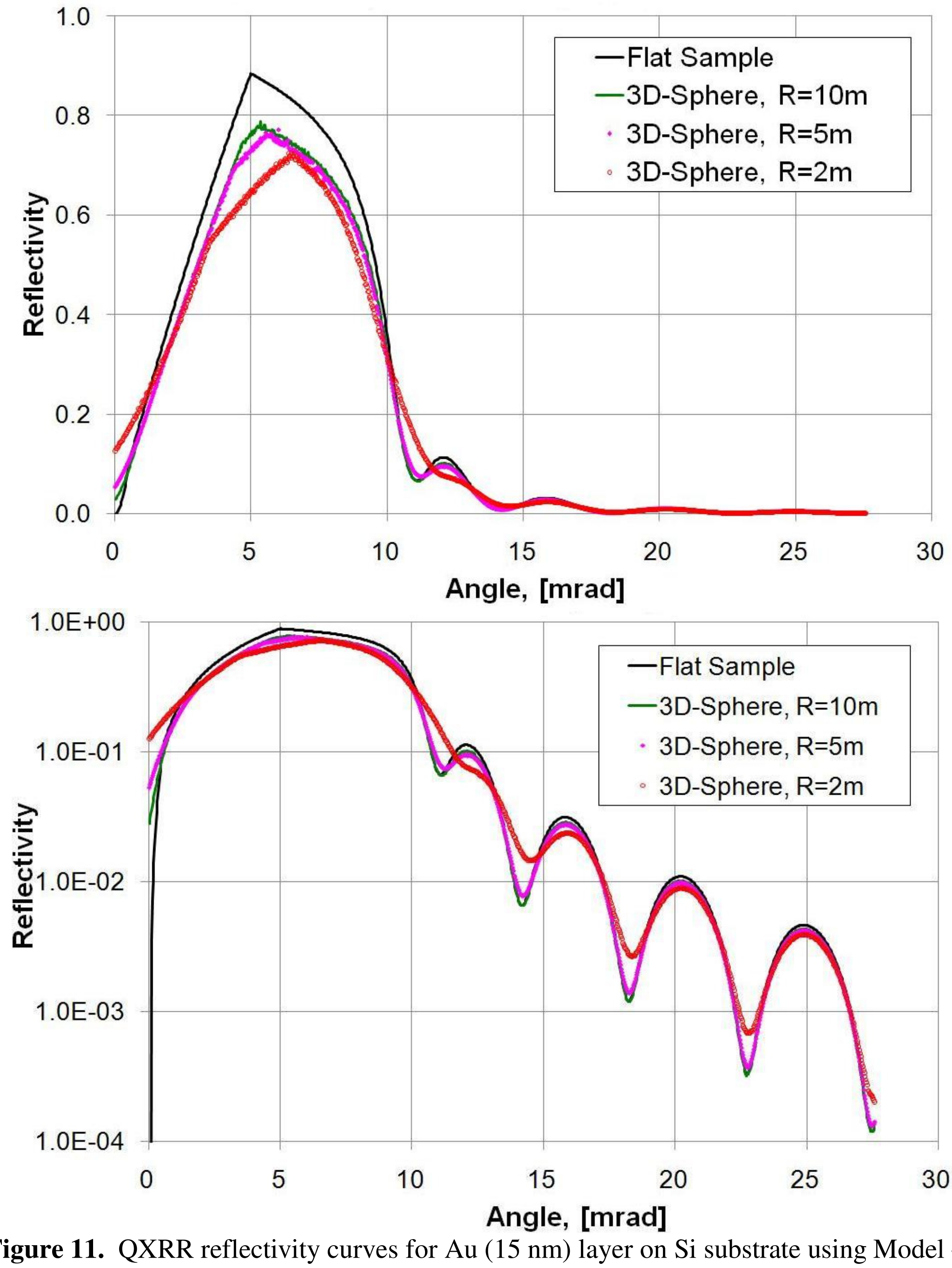

Figure 11. QXRR reflectivity curves for Au (15 nm) layer on Si substrate using Model #4 ($\boldsymbol{E}$ = 8.04 keV, $\boldsymbol{S_L} = \boldsymbol{S_R}$ = 6 mm, $\boldsymbol{H_K}$ = 0.03 mm, roughness of 1 nm).

The third sample modeled was a Ni/C multilayer on a silicon substrate. The calculated reflectivity curves for samples with different radii are shown in Figure 12, in both linear and logarithmic scales.

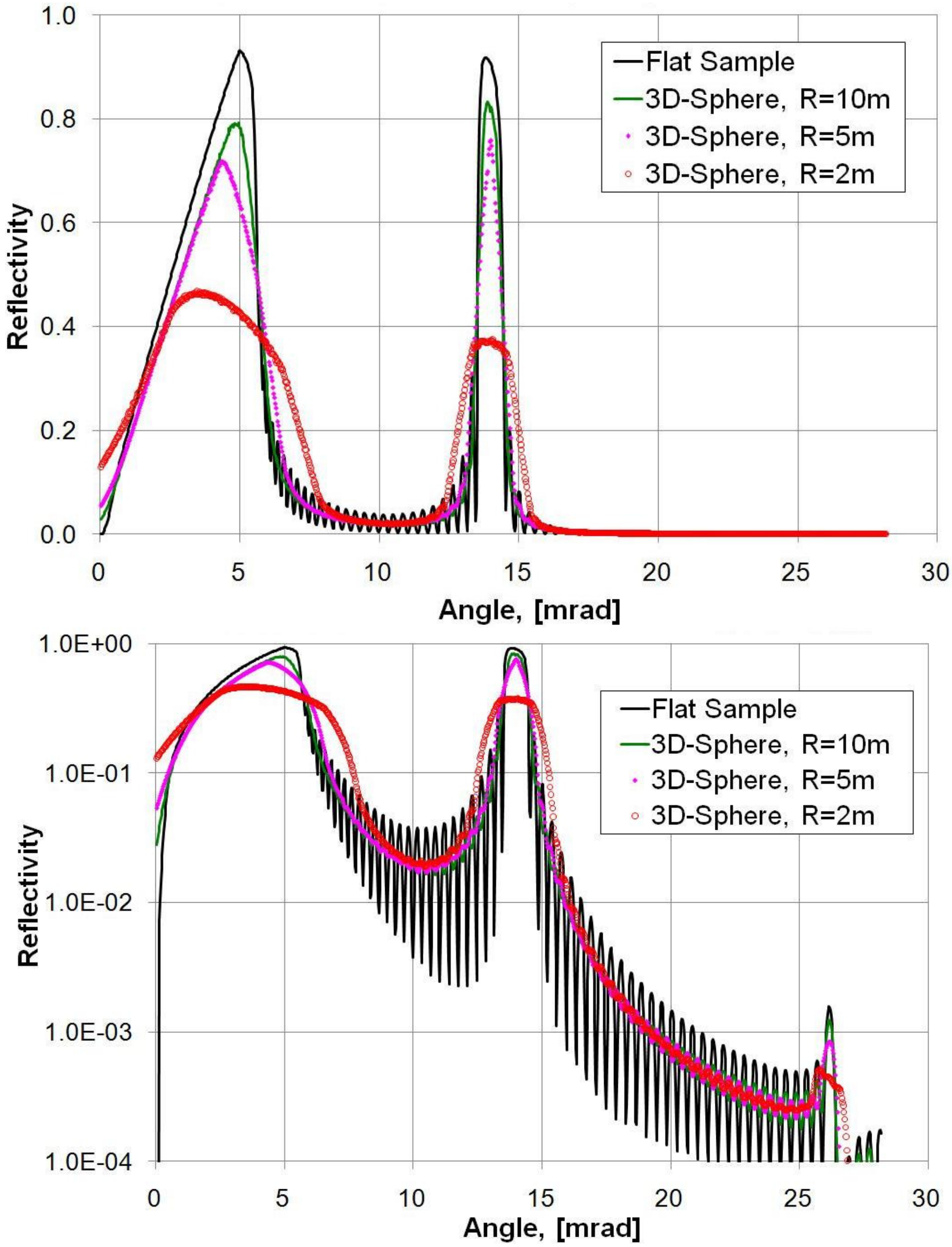

Figure 12. QXRR reflectivity curves for Ni/C multilayer on Si substrate using Model #4 ($\boldsymbol{E}$ = 8.04 keV, $\boldsymbol{S_L} = \boldsymbol{S_R}$ = 6 mm, $\boldsymbol{H_K}$ = 0.03 mm, no roughness).

The following effects can be observed with the increase in curvature of the sample (i.e., with decrease of the sample radius):

- There is a change in the region around the critical angle, which could be misinterpreted as change in the critical angle (e.g., sample density or roughness change);
- The amplitude and position of the high-frequency fringes (intensity oscillations) around the Bragg peak are changed, and, for small sample radii, the high-frequency fringes disappear almost completely;
- The amplitude and width of the Bragg peak are changed;
- For angles smaller than the critical angle, reflectivity is reduced.

Again, the results show that sample curvature can significantly influence the interpretation of results from QXRR, and, thus, modeling of the sample curvature should be included in fitting of experimental results.

The overall conclusion is that the distortion of the reflectivity curve is larger at smaller incident angles (i.e., the smaller the incident angle, the larger the distortion). This effect was anticipated even before performing the modeling for curved samples. This explains why he reflectivity curve for the Ni/C multilayer around the critical angle is more distorted than that for the Au layer on Si (e.g., the critical angle for Au layer is about twice that of the critical angle for the multilayer, and at higher angles the distortion is smaller).

5. Conclusions

Quick x-ray reflectivity is a very promising new surface and interface analysis technique, which will permit nano-scale studies of fast processes such as the time evolution of chemical, thermal, and mechanical changes at the surface and interfaces of different materials. The existing models for interpretation of x-ray reflectivity data are derived for the classical x-ray reflectivity setup, where both the incident and the detected beams are restricted by slits, and cannot be directly applied to quick x-ray reflectivity simulations. This paper has presented and discussed models for evaluation of the contribution of sample curvature to the measured signal for QXRR. Such simulations are very important to interpretation of the results from QXRR measurements, because sample curvature can cause changes in the shape of the x-ray reflectivity curve that are similar to the changes introduced by the sample structural parameters such as density, roughness, layer thickness, etc. The overall conclusion is that sample curvature has much stronger influence on the shape of the reflectivity curve for QXRR than the contribution of the diffuse scattering. Model #4 (3D spherical) was proposed and should be included in the fitting of experimental results from QXRR of curved samples in order to improve the reliability of the calculated structural parameters of the samples (density, layer thickness, roughness, etc.). However, applying this model for fitting experimental data has to be done carefully as one has to consider the possibility that the surface of a liquid sample can have a varying radius of curvature depending on the position of each point of interest. Future work will include incorporating the proposed models in the fitting procedure of the RefleX software and applying the models for fitting experimental data from QXRR of transient processes.

Acknowledgment

This study was done under a collaborative research project between AECL-Canada and NIMS-Japan on x-ray physics and industrial radiography.

References

[1] K. Sakurai and M. Mizusawa, Japanese Patent No. 3903184 (Issued: 19 Jan. 2007, Filing: 9 Feb. 2004)
[2] K. Sakurai, M. Mizusawa and M. Ishii, *Trans MRS-Japan*, **32**, 181-186 (2007).
[3] K. Sakurai, M. Mizusawa, M. Ishii, S. Kobayashi and Y. Imai, “Instrumentation for x-ray reflectivity in micro area: present status and future outlook”, *Journal of Physics: Conference Series*, **83**, 012001, (2007).
[4] A. Naudon, J. Chihab, P. Goudeau and J. Mimault, “New apparatus for grazing x-ray reflectometry in the angle-resolved dispersive mode”, *J. Appl. Cryst.,* **22**, 460-464 (1989).
[5] A. Naudon, *Analusis (France)*, **18,** I22-I22 (1992).
[6] J. Chihab and A. Naudon, *J.de Phys. III* (France), **2,** 2291-2300 (1992).
[7] U. Niggemeier, K. Lischka, W. M. Plotz and V. Holy, *J. Appl. Cryst.,* **30,** 905-908 (1997).
[8] L. N. Koppel, US patent No. 5619548, “X-ray thickness gauge” (1997).
[9] P. Albouy and P. Valerio, “A motionless x-ray reflectometer for air/liquid interface based on Naudon’s design: example of application”, *Supromolecular Science*, **4**, 191-194 (1997).
[10] K. Stoev, V. Samson, M. Mizusawa and K. Sakurai, “Calculation of diffuse scattering in quick x-ray reflectometry”, **45 Annual Conference on X-Ray Chemical Analysis**, Nov. 5-6, 2009, Osaka, Japan.
[11] K. Stoev, J. Knoth and H. Schwenke, “X-ray reflectivity simulation software”, **7th German-Japanese Workshop on Chemical Information**, April 10-12, 1997, Nara, Japan, (http://inaba.nims.go.jp/G-J/report/stoev.html).
[12] M. Mizusawa, K. Stoev and K. Sakurai, **2002 Photon Factory Activity Report Part B**, 2003, #20, p.64
[13] S. Stepanov, “TER_SL on-line calculation tool for x-ray specular reflectivity”, http://sergey.gmca.aps.anl.gov/TER_sl.html.
[14] LBNL x-ray reflectivity online calculation tool, http://henke.lbl.gov/optical_constants/mirror2.html.
[15] P. Kirkpatrick and A. Baez, "Formation of optical images by x-rays", *JOSA*, **38**, 766 (1948).
[16] J. Underwood, A. Thompson, Y. Wu and R. Giauque, "X-ray microprobe using multilayer mirrors", *Nucl. Instr. and Meth. in Phys. Research*, **A266**, 296 (1988).
[17] F. Bridou, "Curvature effect in grazing x-ray reflectometry", *J Physics III France*, **4**, 1513-1522 (1994).